AIAA JOURNAL
Vol. 46, No. 2, February 2008

Transient Growth and Transition Induced by Random Distributed Roughness

Robert S. Downs III,* Edward B. White,† and Nicholas A. Denissen*
Texas A&M University, College Station, Texas 77843

DOI: 10.2514/1.31696

Recent experiments on transient disturbances generated by three-dimensional roughness have used spanwise-periodic arrays of geometrically simple cylindrical roughness elements. Connecting these laboratory experiments to more realistic situations requires the study of surfaces with distributed roughness. This is accomplished in this work by numerically generating quasi-random rough surfaces and manufacturing these surfaces using rapid-prototyping technology. Measurements of the disturbances that the rough surface creates in a Blasius boundary layer are obtained for three test configurations corresponding to roughness-based Reynolds numbers of $Re_k = 164$, 227 and 301. The two lower values give laminar flow; the highest value results in localized transition approximately 140 mm downstream of the leading edge of the roughness. All three configurations exhibit transient growth of steady disturbances. Unsteady fluctuations indicate that transition in the $Re_k = 301$ configuration is likely an example of a bypass transition mechanism in which the unsteady-disturbance growth outpaces the stabilizing relaxation of the steady flow. Measurements above the roughness surface in the $Re_k = 227$ configuration provide a phenomenological model for distributed receptivity.

Nomenclature

$A_{n,m}$	=	amplitude coefficients for the roughness surface
E_{rms}	=	total disturbance energy
$E_{\lambda_k/m}$	=	disturbance energy for spanwise wavelength mode m
H	=	boundary-layer shape factor, δ^*/θ
$h(x, z)$	=	roughness height relative to the plate surface
k	=	maximum roughness height (1 mm)
M	=	spanwise dimension of amplitude and phase coefficient arrays
m	=	spanwise index for amplitude and phase coefficients
N	=	streamwise dimension of amplitude and phase coefficient arrays
n	=	streamwise index for amplitude and phase coefficients
Re_k	=	Reynolds number based on maximum roughness height, $U(k)k/\nu$
Re_δ	=	Reynolds number based on boundary-layer thickness, $U_\infty\delta/\nu$
Re'	=	unit Reynolds number, U_∞/ν
$\bar{U}$	=	basic-state velocity
$U(k)$	=	boundary-layer velocity at the roughness height k
U_∞	=	freestream velocity
U'	=	steady-disturbance velocity
U'_{rms}	=	spanwise root-mean-square steady-disturbance velocity
u	=	streamwise boundary-layer velocity
u'	=	boundary-layer fluctuation velocity
u'_{rms}	=	temporal root-mean-square fluctuation velocity
x	=	streamwise coordinate relative to the physical leading edge
x_k	=	streamwise midpoint of the roughness (450 mm)
x_{vle}	=	streamwise coordinate relative to the virtual leading edge
x^*	=	dimensionless streamwise coordinate, $(x - x_k)/\delta_k$
y	=	wall-normal coordinate
z	=	spanwise coordinate
β	=	dimensionless spanwise wave number, $\beta^*\delta$
β^*	=	spanwise wave number, $2\pi/\lambda$
δ	=	boundary-layer thickness, $[(x - x_{\text{vle}})/Re']^{1/2}$
δ^*	=	displacement thickness
η	=	wall-normal Blasius coordinate, y/δ
θ	=	momentum thickness
λ_k	=	roughness wavelength (32 mm)
ν	=	kinematic viscosity
$\phi_{n,m}$	=	phase coefficients for the roughness surface

Subscripts

k	=	relating to the roughness
m	=	spanwise wavelength mode

Received 18 April 2007; revision received 30 July 2007; accepted for publication 10 September 2007.

*Graduate Research Assistant. Student Member AIAA.
†Associate Professor. Senior Member AIAA.

I. Introduction

BOUNDARY-LAYER transition over rough surfaces has been of interest for many years. However, in spite of wide-ranging studies of roughness effects, surprisingly little is known about how randomly distributed three-dimensional (3D) roughness affects transition in two-dimensional (2D) low-speed boundary layers. Although work to understand roughness was performed in the 1950s and earlier [1–3], reviews from the 1990s (e.g., [4,5]) mainly focus on what is *not* known about roughness and transition in these seemingly simple conditions.

Recently, the development of transient growth theory [6,7] has provided a framework that is helping to guide and reenergize research on roughness effects in both low-speed and high-speed [8] flows. Transient growth is the first theoretical approach to provide a correct framework for incorporating roughness-induced disturbances into a comprehensive stability theory [7]. The theory describes how a superposition of decaying nonorthogonal modes can bring about a brief phase of disturbance-energy growth. The connection to surface roughness lies with the fact that optimal disturbances (i.e., those that undergo maximum energy growth over a specified time or streamwise distance [9]) are stationary spanwise-varying disturbances [10–13], exactly what roughness can be expected to produce [7]. Despite this obvious connection, a number of challenges remain to be overcome before surface roughness (particularly, randomly distributed 3D surface roughness) can be appropriately addressed from the theoretical and predictive viewpoints that transient growth theory provides.

The experiments presented here provide data intended to help incorporate randomly distributed 3D surface roughness into a theoretical framework. The approach is to manufacture a surface for which the coordinates are randomly generated and to observe how disturbances are generated by this surface, how they grow, and how they bring about transition. There are numerous advantages associated with manufacturing random rough surfaces. These include the ability to reproduce experimental conditions in other experiments and in numerical simulations, as well as the ability to know and control key features of the rough surface's parameters for comparisons with theoretical models. There are also distinct experimental advantages to this approach. For this work, the roughness is spatially extended, but most growth measurements are made over a smooth surface downstream of the roughness. This is a necessary first step that avoids the complication of combined disturbance growth and distributed disturbance accumulation over the roughness. Additionally, however, some measurements are made over distributed roughness, and these provide clues as to the nature of distributed-roughness receptivity.

II. Background

When considering how roughness might affect transition, the transition roadmap is a useful means of framing possible scenarios. The roadmap was introduced by Morkovin [14] as a means of summarizing what is known and unknown about transition. Numerous clarifications have brought the roadmap to the form given in Fig. 1 [15]. The roadmap gives a simplified overview of the scenarios by which boundary-layer transition can occur. All begin with receptivity, the process by which disturbances enter a boundary layer and provide the initial conditions for disturbance growth [14]. This growth may come about due to eigenmode growth, transient growth, or some combination of these, leading to breakdown and turbulence. Or, when the initial disturbances are large, the linear-growth mechanisms may not come into play and some form of bypass transition can result. Recent discussions on various aspects of the roadmap are contained elsewhere (e.g., [16,17]).

Roughness is captured in the transition roadmap in various ways, depending on the roughness type. It is usually considered to be one of the "environmental" disturbances to which the flow may be receptive. Roughness might also modify the rate or nature of eigenmode growth along path A by, for instance, changing the surface boundary condition.

Roughness is frequently categorized as being a two-dimensional (i.e., spanwise invariant) surface protuberance, an isolated three-dimensional surface protuberance, or a distributed field of 3D elements, which may be regularly or randomly placed. Two-dimensional roughness is the simplest type to understand from both experimental and theoretical viewpoints. Since the 1950s, transition correlations have been used to determine how increasing 2D roughness heights can accelerate transition [3,18,19]. The growth rates of Tollmien–Schlichting (TS) waves are affected by the combination of 2D roughness and freestream acoustic waves [16,20]. So increasing the amplitude of 2D roughness generates larger TS waves and hastens transition.

Isolated 3D roughness has resisted the detailed theoretical treatment that has been achieved for 2D roughness. Starting in the late 1950s, 3D roughness was observed to be "more critical" than 2D roughness [3]. This means that when the roughness-based Reynolds number Re_k of the elements is below some critical value between 600 and 900, the roughness appears to have no impact on transition, but when an element's Re_k exceeds $Re_{k,\mathrm{crit}}$, bypass transition occurs somewhere downstream of the element. As Re_k becomes supercritical, transition is observed to move rapidly forward toward the element. Of course, this simple correlation-based approach ignores the role the roughness might have in scenarios in which it is not the dominant feature.

Recently, 3D isolated-roughness elements have been of interest in the context of experimental work on transient growth [21–25]. One of these experiments by Ergin and White [25] gives detailed information on the supercritical Re_k bypass. It was proposed that the critical nature of isolated 3D elements results from a competition between a distorted steady flow that rapidly relaxes toward Blasius conditions and growing instabilities of the distorted flow. Direct numerical simulations of Ergin and White's experiment have been performed by Rizzetta and Visbal [26], who observed similar behavior.

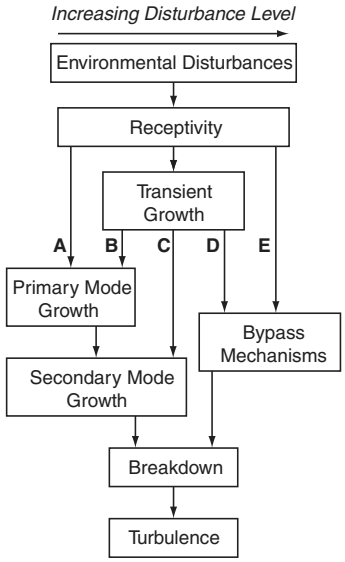

Fig. 1 Transition roadmap, adapted from [15].

The transition scenario observed by Ergin and White [25] and Rizzetta and Visbal [26] can be classified as following path D on the transition roadmap (Fig. 1). The roughness element establishes initial conditions for transient growth, but this is quickly overwhelmed by growing Kelvin–Helmholtz instabilities in the distorted wake of the roughness element. In the subcritical Re_k cases, transition does not occur in the measurement domain [25,26], and the eventual transition is likely to follow the path-B scenario. In this context, the path-B scenario is one in which the steady transient disturbances modify the basic state in which TS waves grow, increasing their growth rates.

Compared with 2D and isolated 3D roughness, little is known about the mechanisms through which distributed 3D surface roughness affects transition. One reason is that before the development of transient growth theory, a successful theoretical basis for understanding distributed subcritical roughness did not exist. Attempts were made to understand random roughness both as a disturbance generator and mean-flow modifier [4,27], but neither approach proved to capable of explaining the observed phenomena. Another reason is that 3D roughness is a parameter-rich topic, and no clear canonical problem exists that focuses research efforts on a single tractable problem.

Most work on the distributed-roughness problem has been experimental. Early efforts were devoted to transition correlations. A key experiment of that period was by von Doenhoff and Horton [28], who roughened a 2D airfoil by adhering grit particles to the surface using lacquer. This approach produced a sparse field of roughness elements, which is not typical of all rough surfaces. The approach did have the good feature of not including a 2D step at the leading edge of the rough patch. (Many other 3D roughness experiments have used sandpaper roughness, and the leading and trailing edges of the patch complicates the analysis of these experiments [5].) With their approach, von Doenhoff and Horton [28] found the roughness to cause transition when the largest roughness elements in the field exceeded the same critical Re_k threshold that applies for isolated elements. When none of the elements exceeded $Re_{k,\mathrm{crit}}$, no effect was observed.

Moving into the 1980s, work shifted toward understanding the mechanisms by which distributed roughness affects transition. This period contained key contributions by Reshotko and Leventhal [29], Kendall [30], and Corke et al. [31]. Reshotko and Leventhal [29]

performed an experiment in which sandpaper sheets provided distributed roughness. Their measurements included mean and fluctuating streamwise velocity measurements in regions upstream of TS waves' first neutral point. Their measurements did not identify a destabilizing mean-flow profile as had been expected, but they did reveal growing low-frequency disturbances. These disturbances were not understood at the time but are now thought to be transient growth [7]. Simultaneously, Kendall [30] performed experiments using isolated and arrayed 3D roughness elements as well as a distributed-roughness field. Kendall's isolated elements generated stationary disturbances that are also now recognized to have undergone transient growth [24]. Some similar features were observed for the distributed roughness, but it is not clear to what extent pressure variations over the roughness patch might have affected these results.

The experiments by Corke et al. [31] focused on how distributed roughness affects TS-wave development in the supercritical region past the waves' first neutral point. The experiments revealed TS waves that grew faster in the presence of roughness than without. The reason for the increased growth rate was not obvious, because inflectional mean-flow profiles were not observed. Additionally, the experiments also showed the roughness to enhance the three-dimensionality of the TS waves. This is thought to have accelerated the onset of secondary instabilities and breakdown. In these respects, the Corke et al. experiments fall within the path-B scenario of the transition roadmap. TS waves are the disturbances that bring about transition, but they do so in a manner that is strongly affected by the 3D transient disturbances generated by the roughness.

Working from this background, the objective of the present experiment is to reveal the behavior of disturbances induced by randomly distributed 3D surface roughness and to do so in the context of recent theoretical developments. Of particular interest is whether the steady disturbances generated by roughness undergo transient growth. It is expected that they do. However, previous experiments that verified that roughness leads to transient disturbance growth (e.g., [22]) used simple roughness shapes that produced simple disturbance spectra. Here, a complicated roughness field with multiple distributed peaks and valleys will lead to a richer spanwise wave-number spectrum, and it is not known how this will affect the resulting disturbance evolution. It is known that receptivity is a key feature that determines the degree of suboptimal transient behavior [22,24] , and distributed random roughness certainly presents a complicated receptivity problem. Also of interest is the breakdown mechanism when the roughness becomes large. The historical transition correlation for sparse random roughness predicts that when Re_k exceeds 600, transition will occur [28]. The mechanism for this transition is thought to be the same as for isolated elements. It is unknown whether the mechanisms associated with isolated-roughness transition will be observed in a more complicated distributed-roughness case in which multiple roughness peaks and valleys could interfere with the flow's development around any particular roughness feature.

III. Experiments and Data Analysis

The experiments are performed in the Case Western Reserve University wind tunnel, a low-speed open-return tunnel. Realistic surface roughness is approximated using a spanwise-periodic array of roughness patches. Rapid-prototyping technology is used to manufacture a sheet of roughness that is incorporated onto a flat plate. Streamwise velocity measurements are made downstream of and over the surface of the roughness. These measurements are used to determine how the steady disturbances are generated by the roughness and how they evolve in the streamwise direction.

A. Experimental Setup

The CWRU wind tunnel is designed specifically for boundary-layer stability experiments; at nominal test speeds, the tunnel develops a streamwise turbulence intensity of approximately 0.09% of the freestream speed (1-Hz high-pass filter). It has been shown that slightly less than half of this fluctuation intensity is due to acoustic disturbances, resulting in a turbulent fluctuation level of 0.05%. Velocity measurements are made using two 2.5-μm-diam hot-wire probes. Streamwise velocity measurements are made concurrently in the boundary layer and the freestream. The velocity measured by the boundary-layer probe $u(y)$ is normalized on a point-by-point basis by the freestream velocity U_∞ to give a nondimensional boundary-layer velocity. Measurement of the flowfield is accomplished by collecting data in dense 2D grids at varying streamwise locations. The motion of hot-wire probes is controlled by an externally mounted traverse that provides approximately 1200 mm of travel in the streamwise direction x, 190 mm of travel in the spanwise direction z, and 70 mm of travel in the wall-normal direction y. The stepper motors that drive the traverse provide this motion in steps of 3.2, 3.2, and 1.6 μm, respectively.

To incorporate the distributed roughness onto the flat plate, a 230 by 230 mm, 6-mm-thick roughness sheet is constructed that includes the random roughness array. The rough portion of the surface extends above and below the nominal surface level of the sheet. A 3-mm-thick, 12-mm-wide border on the roughness sheet allows it to be secured to the flat plate using an aluminum frame. Figure 2 shows a diagram of this assembly. The frame has two purposes: It secures the roughness sheet to the plate and provides a smooth ramp from the plate surface to the roughness surface. The front portion of the frame sits in a shallow recess in the flat-plate surface that has been used to hold recessed sandpaper for similar experiments [21]. Here, it allows a continuous interface between the plate and the frame while maintaining a suitably thick frame leading edge. The leading edge of the frame's linear ramp begins 100 mm downstream of the plate's leading edge; its thickness increases to the roughness sheet's thickness over a distance of 148 mm. Immediately aft of the ramp is a 186-mm-long, smooth, flat section (composed of the frame and the upstream section of the roughness sheet) before the roughness starts. Aft of the 32-mm-long roughness is approximately 200 mm of smooth surface for downstream measurements. The trailing edge of

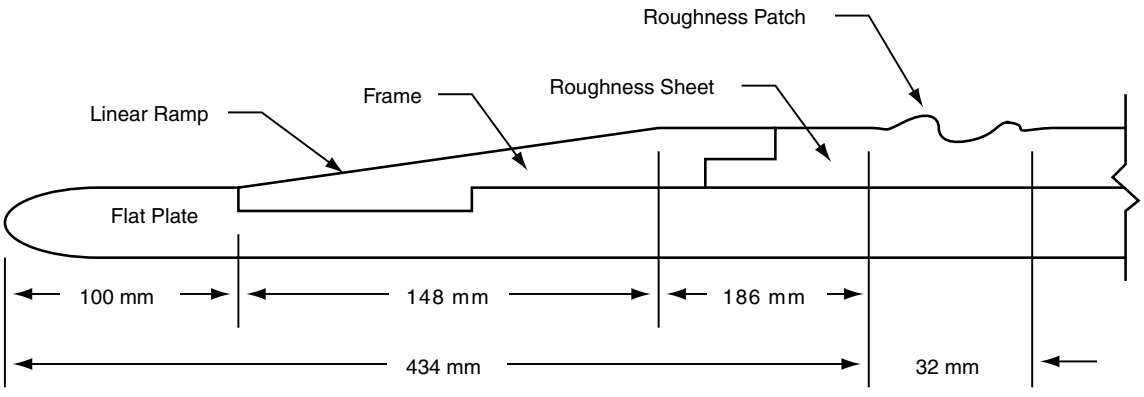

Fig. 2 Schematic diagram of the flat plate, roughness sheet, and frame (not to scale).

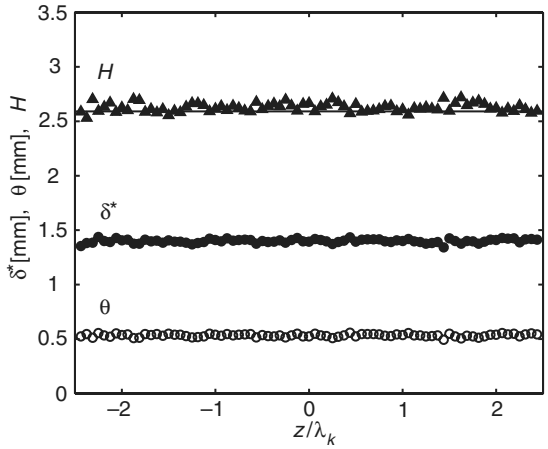

Fig. 3 Boundary-layer integral quantities at $x = 425$ mm.

the frame as well as its sides are blunt; no attempt is made to provide a continuous interface between the frame and the plate surface at those edges. Additional details regarding this setup are available in [32].

The flat plate to which the roughness assembly is mounted is 1 m long, 10 mm thick, and spans the tunnel's 710-mm-square cross section. The leading edge of the plate is elliptical in shape. A hinged trailing-edge flap is used to ensure that the incoming flow stagnates on the test side of the plate. In preparation for these experiments, with the roughness sheet installed, the plate is aligned such that the streamwise average value of the boundary-layer shape factor H is 2.61 for a freestream speed of 9.3 m/s. This value falls within an acceptable range [33] of the theoretical zero pressure gradient value of $H = 2.591$. At the same velocity, the virtual leading-edge location x_{vle} is found to be 78 ± 17 mm and the unit Reynolds number Re' is computed to be $(513 \pm 22) \times 10^3$ m^{-1}. The uncertainties in these quantities are slightly larger than those quoted for previous experiments (e.g., [24,25]), due to the nature of this experimental setup. Although it was possible in previous experiments to measure alignment data before the roughness elements were adhered to the flat plate (thus using the entire span for these measurements), alignment data for the present experiments could only be measured in spanwise locations in which there was no roughness. Because fewer data points were available for computing the values of x_{vle} and Re', the respective uncertainties in these quantities are higher.

Boundary-layer thicknesses and shape-factor measurements are also used to ensure that the flow just upstream of the roughness is spanwise-uniform. To correctly quantify the effect of the roughness on the measured flowfield, any disturbance generated by the interface of the roughness frame and the roughness sheet should be minimal. To ensure that this is true, boundary-layer profiles are recorded at many spanwise locations for $x = 425$ mm (9 mm upstream of the leading edge of the roughness). Shape factors are computed from these profiles and shown in Fig. 3. The variance of δ^*, θ, and H are deemed to be acceptable, and the slope of each of these variables across the span is negligible.

B. Roughness Design

Spanwise-periodic quasi-random roughness is used to mimic real surface roughness. Previous experiments [24,25] that used spanwise arrays of cylindrical roughness elements found spanwise periodicity to be useful for spatial phase-locked averaging of the velocity measurements. To achieve spatial periodicity here, a roughness array with seven identical patches of roughness is designed. Of these seven, five are in the range of the hot-wire traverse; the two outside patches ensure periodicity. Given the spanwise range of the hot-wire traverse (190 mm), the roughness array wavelength λ_k is selected to be 32 mm. The roughness patches are designed to contain the fundamental wavelength λ_k and its first ten harmonics. The streamwise length of each roughness patch is also limited to 32 mm. Relative to the physical leading edge of the flat plate, the roughness extends from $x = 434$ to 466 mm in the streamwise direction; the streamwise midpoint ($x = 450$ mm) is denoted as x_k. This range of x locations corresponds to boundary-layer-scale Reynolds numbers of $Re_\delta = 452$ to 470, 533 to 543, and 626 to 638 for the three test cases ($Re_k = 164$, 227, and 301), respectively. These values all fall above $Re_\delta = 302$, the minimum critical Reynolds number for TS-wave growth. Thus, it is possible that TS waves are growing in the experimental domain.

The Blasius boundary layer has an optimal disturbance, for which the dimensionless spanwise wave number β is 0.45 [11–13]. Based on the boundary-layer thickness at the streamwise midpoint of the roughness $\delta_k = [(x_k - x_{\text{vle}})/Re']^{1/2}$, λ_k corresponds to $\beta_k = 0.17$ for the $Re_k = 227$ case. That is, the roughness patches are periodic over a length that is about three times the optimal wavelength. Thus, $m = 3$ is the spanwise mode that is closest to the optimal spanwise wavelength at the streamwise midpoint of the roughness. For the $Re_k = 164$ configuration, $\beta_k = 0.19$; for the $Re_k = 301$ configuration, $\beta_k = 0.16$.

A randomly rough surface is modeled as a series of cosine functions with randomly distributed amplitudes $A_{n,m}$ and phases $\phi_{n,m}$ that are chosen from normal and uniform distributions, respectively. Thus, the surface height with respect to the plate surface is given by

$$h(x,z) = \sum_{n=1}^{N}\sum_{m=1}^{M} A_{n,m}\cos(2\pi nx/\lambda_k + 2\pi mz/\lambda_k + \phi_{n,m})$$

where $N = M = 10$. To limit the minimum roughness wavelength to $\lambda_k/10$, amplitude coefficients with $n^2 + m^2 > 10^2 + 1$ are set to zero. A graphical representation of the amplitude coefficients is shown in Fig. 4. The largest amplitude values are summarized in Table 1. The top three values correspond to the $m = 4$ spanwise component; this is not intentional, but rather a result of the random selection process.

It is desired that the roughness elements not cause a bypass transition at a nominal freestream speed of 10 m/s. Previous

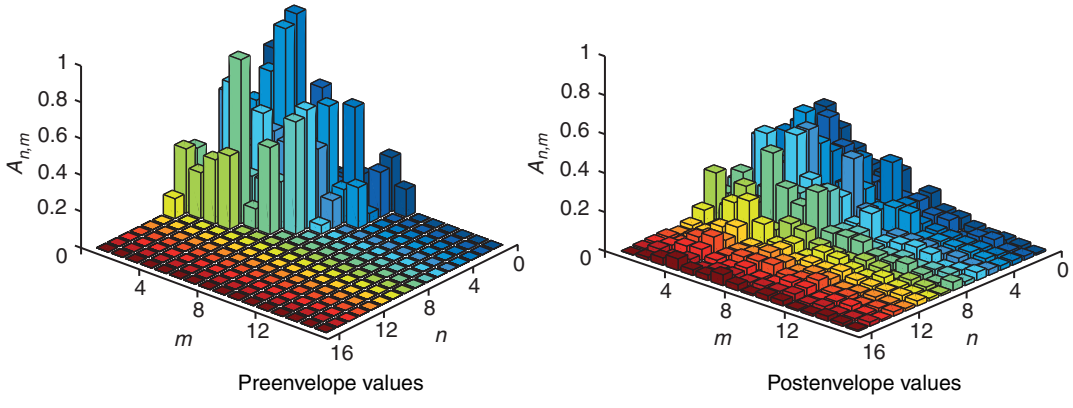

Fig. 4 Normally distributed amplitude coefficients, not including the envelope function (left) and including the envelope function (right).

Table 1 The largest amplitude values (normalized) and associated indices

$A_{n,m}$	n	m
1	3	4
0.953	4	4
0.901	8	4
0.801	1	2
0.684	4	3
0.661	1	1

Table 2 The largest post-envelope amplitude values and associated indices

$A_{n,m}$	n	m
0.469	4	3
0.435	5	4
0.433	6	4
0.395	1	2
0.393	8	4
0.393	2	3

transient growth experiments [34] have shown that the elements should not exceed $Re_k = 250$ (in this particular wind tunnel); this corresponds to a maximum roughness height of about 1 mm at the roughness location. The thickness resolution of the rapid-prototyping process is 0.1 mm so that the surface is reasonably well-resolved. The maximum roughness height results in k/δ_k values of 1.03, 1.10, and 1.15 for $Re_k = 164$, 227, and 301, respectively.

An additional feature that is incorporated into the roughness is a series of 4-mm-wide flat strips that run in the streamwise direction. These so-called roughness flats are included to provide regions in the flow in which the steady disturbance from the Blasius state U' is small. These locations are used to estimate the wall location in traverse coordinates using linear least-squares fits to the wall. As shown in [35], linear fits cannot be used directly behind roughness elements; the roughness flats are critical to this approach. The roughness flats are also used to measure the experimental basic state of the boundary layer. To generate the flats, each roughness patch is multiplied by an envelope function in both the streamwise and spanwise directions. In addition to providing the 4 mm of smooth space between each patch, the envelope function also provides a 4-mm-wide cosine ramp into and out of the rough surface. A schematic drawing of two patches of the numerically generated surface roughness is shown in Fig. 5.

One unintended consequence of applying the envelope function to the roughness is a partial loss of the intended wavelength cutoff. The right side of Fig. 4 shows the amplitude coefficient values that result from the application of the envelope function. The top postenvelope amplitude values are summarized in Table 2; the values are normalized by the highest preenvelope value. Although the envelope function does generate wavelengths shorter than $\lambda_k/10$, 65% of the amplitude content remain in the original longer-wavelength region ($n^2 + m^2 \leq 10^2 + 1$).

C. Data Analysis

The basic-state profile $\bar{U}(\eta)$ is computed by spanwise phase-locked averaging the steady-velocity profiles measured at z locations downstream of the roughness flats. This averaged profile is expected to be least affected by the roughness and most representative of Blasius flow. Likewise, the velocity profiles measured aft of the five roughness patches are also phase-lock-averaged. This process results in a representative flowfield for one roughness patch. The steady boundary-layer disturbance is defined as the deviation from the basic state. Thus, the steady disturbances $U'(\eta, z)$ are computed by subtracting the basic-state profile from each boundary profile behind the roughness. To collapse this steady-disturbance field to a single profile that is representative of the overall flow disturbance that the roughness creates, the rms of the steady-disturbance profiles is taken in the spanwise direction. The result is a single disturbance profile $U'_{\text{rms}}(\eta)$. The total disturbance energy E_{rms} is quantified as the wall-normal integral of this profile squared:

$$E_{\text{rms}} = \int_0^\infty [U'_{\text{rms}}(\eta)]^2 \, \mathrm{d}\eta$$

In practice, this integration is carried out using a simple trapezoidal integration scheme. The upper limit of integration is in the freestream, in which the disturbance profile is close to zero. Typically, η values of 10 to 12 are used for this purpose.

Although the total disturbance energy is a useful means of quantifying the streamwise disturbance evolution, it gives no information as to the behavior of individual spanwise wavelengths in the velocity disturbance field and how these wavelengths might be connected to the roughness. To examine these details, the $U'(\eta, z)$ disturbances are transformed using a spatial Fourier transform in the spanwise direction. This operation is completed using two roughness patches as a spanwise sampling length. Overlapping four such transforms by 50% and complex-averaging the results achieves the optimal reduction in the variance [36]. For a spanwise step size of $\lambda_k/16 = 2$ mm, this results in 32 points per transform. This computation transforms the disturbances in z to the spanwise wavelength domain. Of particular interest are the components at the integer modes: $\lambda/\lambda_k = 1$, $\lambda/\lambda_k = \frac{1}{2}$, $\lambda/\lambda_k = \frac{1}{3}$, etc. Data taken with a small spanwise step size ($\lambda_k/64 = 0.5$ mm) show that although nonnegligible signal power exists in the higher modes (shown in Fig. 6), these disturbances tend to decay over a relatively short streamwise distance (not shown).

After performing the Fourier transforms, the power spectral density (PSD) of the signal is computed. The normalization is such that

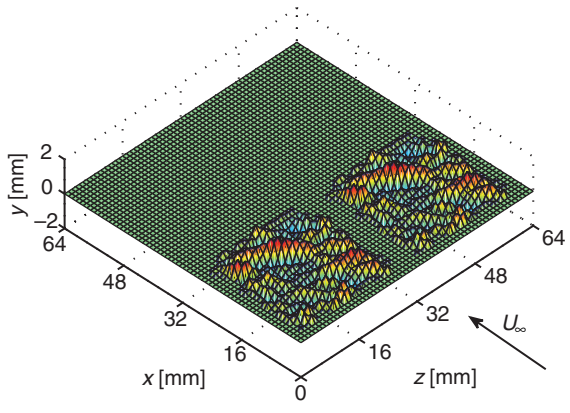

Fig. 5 Numerical representation of two patches of roughness.

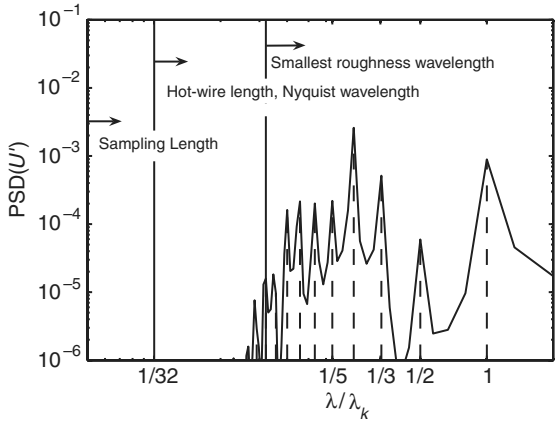

Fig. 6 PSD at $x^* = 82$ and $Re_k = 227$ for a spanwise sampling interval of 0.5 mm ($\lambda_k/64$). The first 12 integer spanwise modes are marked with vertical dashed lines.

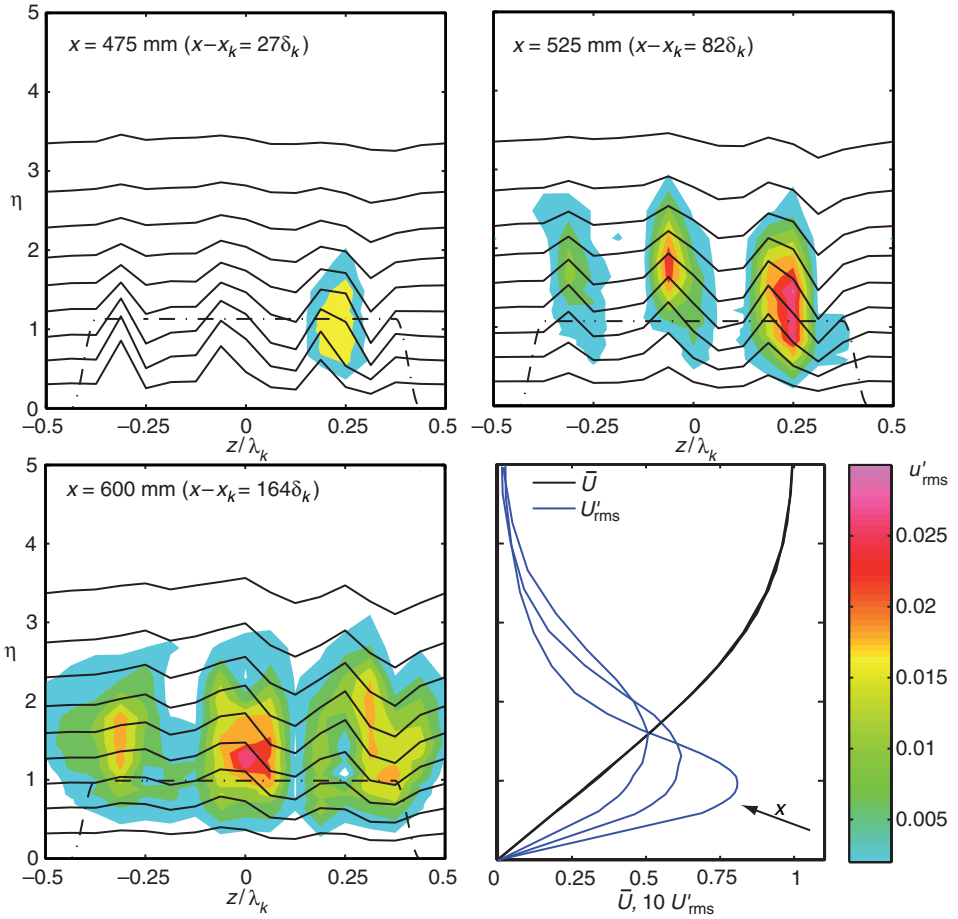

Fig. 7 Velocity contours and fluctuation velocity field for $Re_k = 227$; basic-state and steady-disturbance profiles corresponding to the contour plots are shown in bottom right. Steady velocity contours are at increments of $0.1U_\infty$.

$$[U'_{\text{rms}}(\eta)]^2 = \sum_{m=0}^{\infty} \text{PSD}_m(\eta)$$

The disturbance energy contained in any particular mode can be found in a manner similar to the total disturbance energy. The PSD component of interest is integrated in the wall-normal direction using a simple trapezoidal scheme:

$$E_{\lambda_k/m} = \int_0^{\infty} \text{PSD}_m(\eta)\, \mathrm{d}\eta$$

As a consequence of the PSD normalization, the total disturbance energy is equal to the sum of the disturbance energies in each of the integer modes:

$$E_{\text{rms}} = \sum_{m=0}^{\infty} E_{\lambda_k/m}$$

IV. Results and Discussion

For these experiments, three different roughness-based Reynolds numbers Re_k are investigated. Because the same sheet of roughness is used for all cases, the Reynolds number is changed by varying the freestream velocity. For better comparison of the three test configurations, a dimensionless streamwise coordinate is defined as $x^* = (x - x_k)/\delta_k$, where x_k is the streamwise midpoint of the roughness (450 mm, or $x^* = 0$). The three test configurations use freestream speeds of 7.5, 9.3, and 11.5 m/s, which correspond to Re_k values of 164, 227, and 301, respectively. These values are based on the undisturbed velocity at the roughness location and the maximum roughness height. The $Re_k = 164$ and 227 cases are fully laminar, whereas the $Re_k = 301$ case becomes turbulent approximately 140 mm downstream of the leading edge of the roughness patches (this corresponds to a dimensionless location of $x^* = 144$).

A. Laminar Configurations, $Re_k = 227$ and 164

The steady-disturbance profiles $U'_{\text{rms}}(\eta)$ and the basic-state profiles $\bar{U}(\eta)$ for the $Re_k = 227$ case are shown in the bottom right corner of Fig. 7 for $x^* = 27$, 82, and 164 ($x = 475$, 525, and 600 mm, respectively). At $x^* = 27$, 9 mm aft of the trailing edge of the roughness, the maximum U' is approximately 0.08. This is the largest value observed for $Re_k = 227$; the disturbance magnitudes decrease with increasing streamwise distance. At $x^* = 82$, the magnitude has fallen to about 0.06. At $x^* = 164$, the magnitude has fallen to approximately 0.05. However, as its maximum amplitude decreases, the steady-disturbance profiles broaden in the wall-normal direction as they move downstream. This broadening is accompanied by an increase in the vertical distance between the wall and the peak of the disturbance profile. These observations are consistent with measurements of stationary transient disturbances initiated by arrays of isolated-roughness elements [22,24].

Another useful perspective for visualizing the boundary-layer disturbances is streamwise velocity contours in wall-normal/spanwise planes; such plots are shown in Fig. 7. These plots show isovelocity contour lines for one phase-lock-averaged disturbance field. The dashed lines represent a projection of the envelope function that gives the maximum roughness height. This projection is normalized by δ at all x locations. In addition to contour lines, the unsteady-fluctuation velocity u'_{rms} fields are also shown in these plots as the color contours. These contours are not phase-lock-averaged, but rather represent the middle roughness patch.

The top left corner of Fig. 7 shows the velocity contours at $x^* = 27$. As evident from the contour lines, the flow is decelerated in

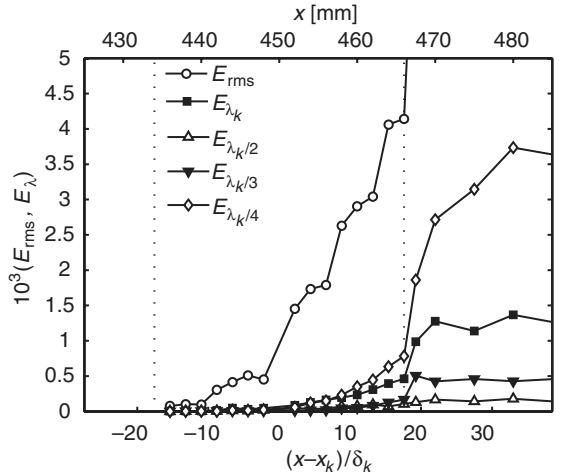

Fig. 8 A selected portion of the disturbance-energy evolution for $Re_k = 227$; the vertical lines indicate the receptivity region (the roughness surface).

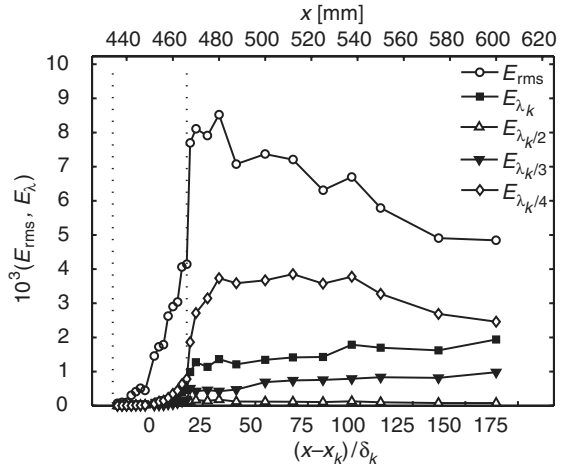

Fig. 9 The complete disturbance-energy evolution for $Re_k = 227$; the vertical lines indicate the receptivity region (the roughness surface).

three distinct zones: near $z/\lambda_k = -0.32$, -0.07, and 0.18. Additionally, the flow appears to be accelerated near $z/\lambda_k = 0.32$. Because of the spanwise juxtaposition of decelerated and accelerated flows in this region, there is a strong spanwise $\partial u/\partial z$ shear near $z/\lambda_k = 0.25$. This shear is accompanied by increased unsteady fluctuations, as is evident in the color contours.

Similar behavior is observed at $x^* = 82$ (shown in the top right corner of Fig. 7). The three decelerated zones and single accelerated zone are persistent and are observed at the same z locations as they were upstream. In each case, the maximum disturbance amplitude has decreased, whereas the disturbances have broadened away from the wall. Although the U' disturbances decayed slightly, there was significant u' growth about each of the three decelerated regions. This evolution continues at $x^* = 164$ (in the bottom left corner of Fig. 7), at which point the u' disturbances may have reached their maximum amplitude and are spreading out away from the originally decelerated zones. Similar to what was observed by Ergin and White [25], the disturbed mean flow is initially unstable to growing u' fluctuations. However, the disturbances do not grow fast enough to lead to turbulence before U' relaxes to the point at which the u' disturbances become stable.

The disturbance energies for the baseline $Re_k = 227$ case are shown in two plots: those measured over the roughness surface (Fig. 8) and the complete evolution downstream of the roughness (Fig. 9). The disturbances over the roughness are much smaller than those downstream and thus do not fit well on the same plot. Figure 8

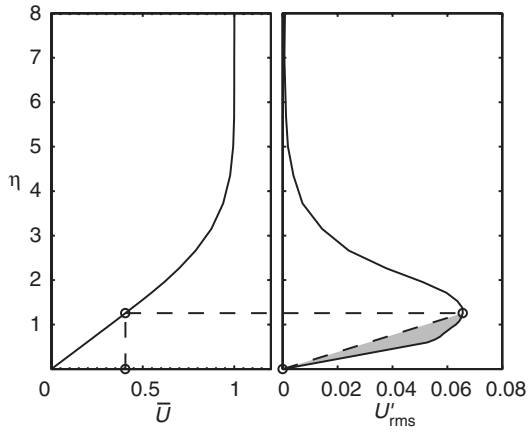

Fig. 10 The systematic error in the U'_{rms} profile introduced by applying a velocity cutoff of $\bar{U} = 0.42$.

shows the total disturbance energy and the disturbance energy in the first four spanwise modes as functions of x^*. The leading edge of the roughness starts at $x^* = -17.6$ and the first measurements are taken at $x^* = -15.4$. As this plot shows, the disturbance energy gradually increases up to the trailing edge of the roughness at $x^* = 17.6$. The disturbance energies in each of the first four spanwise modes increase essentially monotonically, whereas E_{rms} seems to rise through a few quick bursts.

Figure 9 shows the total disturbance energy E_{rms} and the disturbance energy in the first four spanwise modes E_{λ_k}, $E_{\lambda_k/2}$, $E_{\lambda_k/3}$, and $E_{\lambda_k/4}$ as functions of streamwise distance downstream of the roughness surface. This plot shows the disturbance-energy evolution above the roughness and aft of the roughness. E_{rms} undergoes an abbreviated period of transient growth and reaches its maximum 14 mm downstream of the trailing edge of the roughness at $x^* = 33$. From this point through the end of the measurement domain ($x^* = 164$), E_{rms} gradually decays. Its rapid growth from $x^* = 16.5$ to 33 can be almost completely attributed to growth in $E_{\lambda_k/4}$: both increase by approximately the same amount over this distance.

The λ_k disturbance energy exhibits relatively small transient growth over the length of the measurement domain. However, it grows throughout the domain and helps slow the decay of E_{rms} once $E_{\lambda_k/4}$ begins to decay. The $\lambda_k/2$ disturbance energy is quite small relative to the other components and does not appear to change in any significant manner. The $\lambda_k/3$ disturbance energy exhibits the same type of transient growth as the λ_k disturbance energy but at a somewhat lower rate. The most striking transient growth and corresponding decay is evident in the dominant $\lambda_k/4$ disturbance energy. This energy grows by a factor of 4 from its initial value to its maximum at $x^* = 33$. This period of transient growth is followed by decay over the remainder of the measurement domain.

One of the more notable features of Figs. 8 and 9 is the dramatic increase in disturbance energy and the disturbance-energy growth rate that occurs at the trailing edge of the roughness. This could be seen as evidence that distributed roughness suppresses the transient growth of disturbances generated at the upstream portion of the rough surface. However, it is more likely that the discrepancy is due to a subtle change in experimental technique that is used for these two regions. When velocity measurements are made over the roughness surface, a high cutoff velocity is employed to reduce the possibility of physical contact between the hot-wire probe and the roughness surface. For downstream measurements over the flat surface, a velocity cutoff of 20% of U_∞ is used. Once a velocity smaller than this is measured, the probe is moved away from the surface and to the next spanwise point. Over the roughness surface, a velocity cutoff of 42% is used. This value incorporates the boundary-layer thickness in the receptivity region, the maximum roughness height, and an additional wall-normal distance to ensure the safety of the hot-wire probe. As a result, Figs. 8 and 9 may not represent a fair comparison.

To investigate how the measurement technique affects the measured energy, energies are computed at all streamwise locations

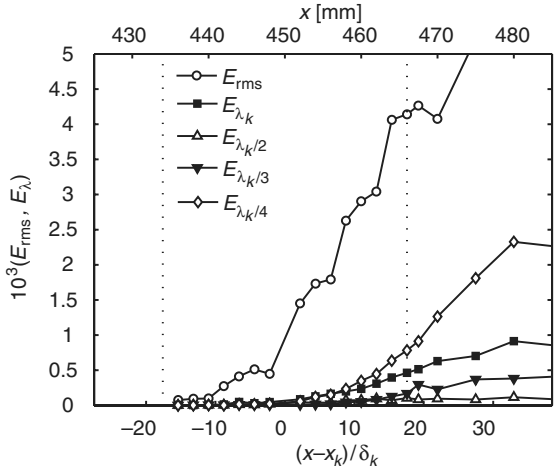

Fig. 11 A selected portion of the disturbance-energy evolution for $Re_k = 227$ using a consistent 42% velocity cutoff.

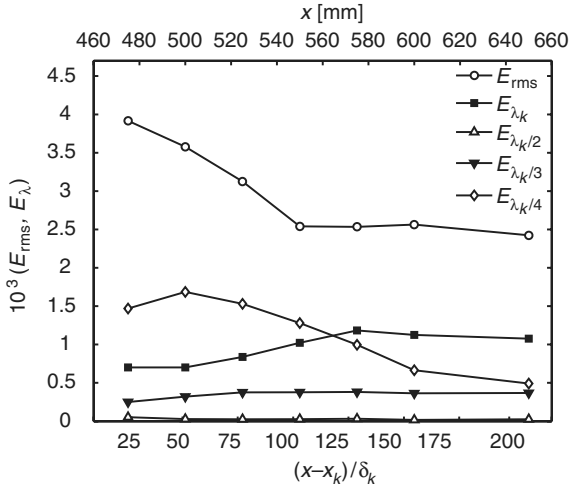

Fig. 12 Disturbance-energy evolution for $Re_k = 164$.

using a 42% velocity cutoff. This higher cutoff increases the uncertainty in the wall location, because less near-wall data are available for extrapolating to the wall location. Additionally, it systematically underestimates energy from the E_{rms} integral. This is illustrated in Fig. 10. The plot on the left shows a typical boundary-layer profile downstream of the roughness. The vertical dashed line represents a 42% cutoff. As the cutoff height is applied to the U'_{rms} disturbance on the right side of Fig. 10 and subsequently extrapolated to zero at the wall location, it is clear that a significant portion of the U'_{rms} profile is neglected. As a result, E_{rms} is systematically lower for this higher cutoff; Fig. 11 verifies the lower energy estimates. However, this figure also shows that the energy jump at the trailing edge of the roughness that is observed in Figs. 8 and 9 is an artifact of the data-collection approach. Using the consistent velocity cutoff (Fig. 11), it is clear that the energy grows smoothly.

The best energy estimates are those that are generated from the most complete data: Figs. 8 and 9. However, Fig. 11 gives a better indication of the energy growth trends as the disturbances move from the rough to the smooth surface. In particular, it appears as if E_{λ_k}, $E_{\lambda_k/4}$, and perhaps $E_{\lambda_k/3}$ grow quadratically over the roughness and linearly for a short distance downstream of the roughness. At the boundary between the quadratic and linear regions, the energy levels and slopes match. A phenomenological argument can be made for this change in energy growth based on the work of White et al. [24]. For some disturbances measured by White et al., the energy downstream of a discrete element grew and decayed as

$$E(x) = a(x - x_k)\exp\left(-\frac{x - x_k}{b}\right)$$

If the disturbance is in the near field of the roughness, $x - x_k \ll b$ and $E \approx a(x - x_k)$. For distributed roughness, if it is assumed that the energy input per unit streamwise distance is constant, then $\mathrm{d}E = C\,\mathrm{d}x$, where $\mathrm{d}E$ is the energy input across a length $\mathrm{d}x$ over the roughness patch. Using this concept and integrating with respect to a dummy variable ξ, the disturbance energy over the roughness ($x < x_{\text{TE}}$) would be

$$E(x) = \int_{x_{\text{LE}}}^{x} Ca(x - \xi)\,\mathrm{d}\xi = \frac{Ca}{2}(x - x_{\text{LE}})^2$$

where the subscripts LE and TE denote the leading and trailing edges of the roughness, respectively. Downstream of the roughness, there is no additional energy input, and so the upper bound of the integral becomes x_{TE} and $x > x_{\text{TE}}$. This yields

$$E(x) = \int_{x_{\text{LE}}}^{x_{\text{TE}}} Ca(x - \xi)\,\mathrm{d}\xi = Ca(x_{\text{TE}} - x_{\text{LE}})(x - x_k)$$

because $x_k = (x_{\text{TE}} + x_{\text{LE}})/2$. As this expression shows, the disturbance energy downstream of the roughness is linear in x and proportional to the streamwise length of the roughness. Additionally, this expression shows consistent linear growth from the middle of the roughness patch. Using these relations to model the energy growth of $E_{\lambda_k/4}$ in Fig. 11 results in fairly good correlations. Notwithstanding the systematic error in E_{rms} and the assumption of constant energy input per unit streamwise distance, there appears to be a basis for the apparent quadratic-to-linear change in E_{λ_k} and $E_{\lambda_k/4}$.

The results for the $Re_k = 164$ are qualitatively similar to the $Re_k = 227$ case. For this reason, detailed U and U' distributions are not shown here, but are available in [32]. The disturbance-energy evolution for the $Re_k = 164$ case is shown in Fig. 12. In this case, the total disturbance energy strictly decays from its maximum value at $x^* = 26$ to slightly more than half of that maximum value at $x^* = 206$. Periods of weak transient growth are observed in the $\lambda_k/4$ and λ_k disturbance energies. As before, the $\lambda_k/4$ disturbance energy is initially the dominant mode, reaching a peak of approximately half of the total disturbance energy by $x^* = 51$ and then decaying to about one-third of its initial value. The λ_k disturbance energy grows over a longer length, reaching its peak of about one-third of the total disturbance energy at $x^* = 155$ and becomes the dominant mode. It too begins to decay in the test region. The $\lambda_k/3$ disturbance energy undergoes slight growth, reaching an apparent plateau at $x^* = 77$. The $\lambda_k/2$ disturbance energy strictly decays. Of the three modes that exhibit transient growth, the trend observed is that longer wavelengths grow and decay over longer streamwise distances. This trend is also observed for the $Re_k = 227$ case. These two configurations invite a discussion of an Re_k^2 energy scaling as in [24] and the U_∞ scaling of [23]; this is addressed at the end of this section.

B. Transitional Configuration, $Re_k = 301$

For the $Re_k = 301$ case, selected steady-disturbance profiles are shown in the bottom right corner of Fig. 13 for $x^* = 29$, 86, and 230 ($x = 475$, 525, and 650 mm, respectively). When compared with the steady-disturbance profiles for the $Re_k = 227$ case, two initial observations can be made. First, as U_∞ (and, consequently, Re_k) is increased, the disturbance amplitudes increase. At $x^* = 26$, the peak amplitude of the U'_{rms} disturbances increases from 0.08 in the $Re_k = 227$ case to approximately 0.105 in the $Re_k = 301$ case (note that these plots represent slightly different dimensionless streamwise locations). As before, as the disturbances move downstream, they move higher into the boundary layer, broaden, and decrease in maximum amplitude. Second, the steady-disturbance profile at $x^* = 230$ has taken on a markedly different shape from the other profiles. This is the manifestation of turbulence that is observed for this case.

Steady isovelocity contour lines and unsteady-fluctuation velocity contours are shown in Fig. 13. At $x^* = 29$ (in the top left corner of Fig. 13), the same three decelerated regions are evident as in the $Re_k = 227$ case, but the magnitude and vertical range of the disturbances is greater than before. This increased level of

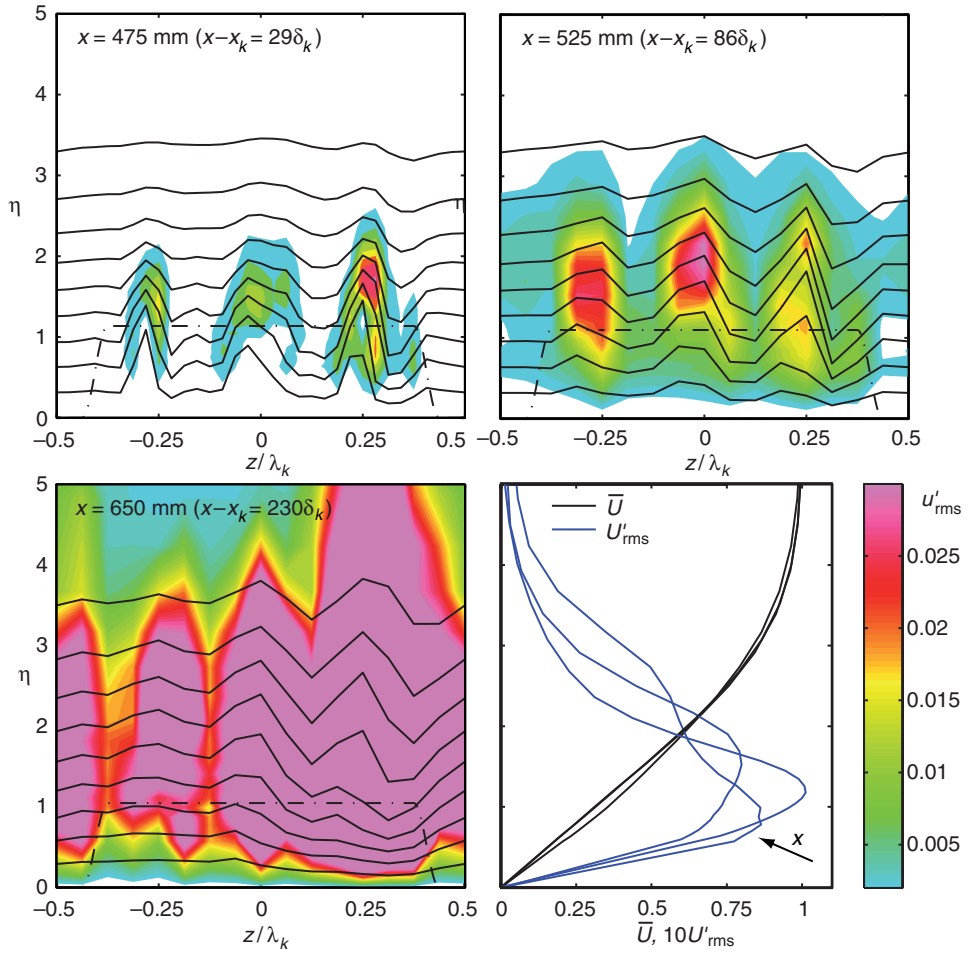

Fig. 13 Velocity contours and fluctuation velocity field for $Re_k = 301$; basic-state and steady-disturbance profiles corresponding to the contour plots are shown in bottom right. Steady velocity contours are at increments of $0.1U_\infty$.

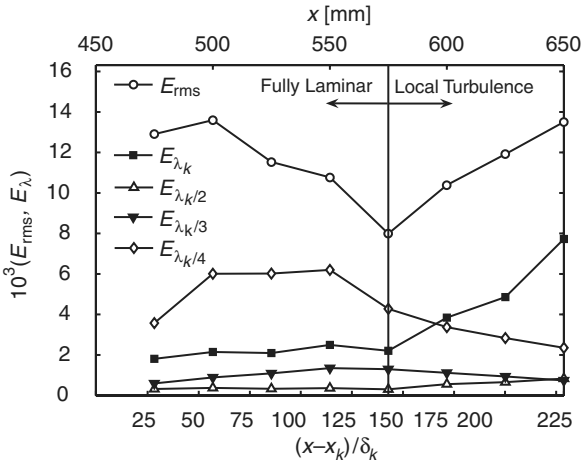

Fig. 14 Disturbance-energy evolution for $Re_k = 301$.

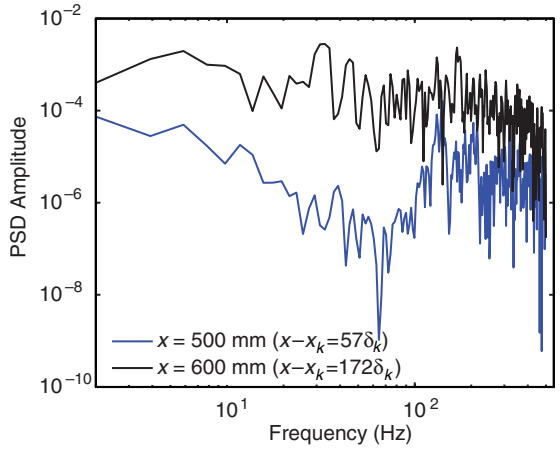

Fig. 15 Temporal power spectral density for the $Re_k = 301$ case at $(x^*, \eta, z/\lambda_k) = (57, 1.9, 0.25)$ and $(172, 1.78, 0.25)$.

disturbance is accompanied by an increased fluctuation intensity, particularly at around $z/\lambda_k = 0.25$. Similar trends are evident at $x^* = 86$; increasing the Reynolds number has the effect of increasing the magnitudes of both U' and u'. Because the unsteady fluctuations are locally unstable in the basic state associated with the distorted steady flow [25], this connection between higher U' and $u'_{\rm rms}$ is to be expected. Moving downstream to $x^* = 230$, the u' fluctuations have grown large enough in magnitude and range to saturate most of the plot. This indicates that localized turbulent bursts are beginning to contaminate the measurement domain. Also, the $\bar{U}$ profile for $x^* = 230$ is beginning to diverge from the upstream laminar basic-state profiles toward a shape indicative of a turbulent boundary-layer profile.

The disturbance energies for the $Re_k = 301$ case are shown in Fig. 14. The laminar region to the left of the vertical line at $x^* = 144$ is considered first. The total disturbance energy grows only marginally between the trailing edge of the roughness and its maximum value that occurs at $x^* = 57$. Thereafter, it decays until turbulent bursts begin at $x^* = 144$. As with the other two configurations, the $\lambda_k/4$ mode is the dominant spanwise disturbance mode. At the trailing edge of the roughness, it represents about one-

third of the total disturbance energy. It continues to grow, whereas E_{rms} decays, and at $x^* = 57$, it represents slightly more than half of the total disturbance energy. Meanwhile, the longer-wavelength modes λ_k and $\lambda_k/3$ have grown slightly and comprise most of the remaining total disturbance energy. The higher modes have all decayed to negligible amplitudes and the $\lambda_k/2$ mode remains at an essentially constant, low amplitude throughout the domain. Because of the localized breakdown to turbulence, only part of the measurement domain can be used for the study of transient growth. However, upstream of $x^* = 144$, the behavior of the disturbance energies appears to be qualitatively similar to that of the other two configurations.

Localized transition is observed to occur aft of $x^* = 144$ for the $Re_k = 301$ case. This occurs first at $z/\lambda_k = 0.25$; this spanwise location corresponds to the largest positive roughness height in the roughness field. The points neighboring $z/\lambda_k = 0.25$ remain highly disturbed, but laminar. This determination is first made using the temporal spectrum of the unsteady-velocity measurements. Two such spectra are shown in Fig. 15 for $x^* = 57$ and 172. These points correspond to a spanwise location of $z/\lambda_k = 0.25$ and wall-normal locations of $\eta = 1.90$ and 1.78, respectively (these are the approximate locations of maximum u'_{rms} at this spanwise location). The $x^* = 172$ spectrum exhibits the characteristics of turbulence, whereas the $x^* = 57$ spectrum is of much lower magnitude. This is confirmed by the contour plots of the fluctuation velocity fields. As shown in Fig. 13, the fluctuation velocity field has saturated the color scale ($u'_{\text{rms}} = 0.03$) at $z/\lambda_k = 0.25$. As the flow moves further downstream, this local turbulence begins to contaminate neighboring areas. Had measurements been made further downstream, it is expected that the flow would become uniformly turbulent across the span and that the spanwise variations of the U and u'_{rms} fields associated with particular roughness features would gradually disappear.

The manifestation of this local turbulence in the steady-disturbance energy is shown on the right half of Fig. 14. In this section of the plot, the disturbance energy appears to undergo additional growth. This is due to the effect of the turbulence on the steady-disturbance profiles; it is not due to transient growth. As shown in Fig. 13, the steady-disturbance profile for $x^* = 230$ has a different shape than any of the other steady-disturbance profiles. This is due to the spanwise juxtaposition of laminar and turbulent flows. By taking the spatial rms in the spanwise direction, the effect of the local turbulence is the lower lobe in the steady-disturbance profile. Because the disturbance energy is the integral of the square of this profile, the addition of this second lobe will markedly increase the value of this integral. Thus, the effect of the local turbulence is an apparent increase in the total disturbance energy. As the turbulence spreads across the span, turbulent mixing will surely decrease spanwise variations in U and hence the steady-disturbance energies.

To determine the nature of the transition mechanism, the streamwise evolution of the u'_{rms} profiles is considered. In [25], there was significant variation in the u' levels behind each roughness element. Here, the use of the manufactured roughness produces better spanwise uniformity (see Fig. 16), and so it is possible to consider spanwise phase-lock-averaged u'_{rms} profiles. Such profiles are shown in Fig. 17 for $z/\lambda_k = 0.25$ and in Fig. 18 for $z/\lambda_k = \pm 0.5$ downstream of the roughness flats. Except for the most upstream position, a single maximum in the u'_{rms} profile downstream of the roughness is observed at approximately $\eta = 2.5$. TS waves typically have fluctuation maxima near $\eta = 1$ and 5, higher and lower than the single location observed here. Although the number and location of the maxima are not foolproof evidence of non-TS breakdown, the fact that TS-like profiles are never observed makes it unlikely. This conclusion is reinforced by the fact that there does not appear to be any unusually high signal power in the unstable TS band of the frequency spectra in Fig. 15 (the unstable TS band for these conditions is approximately 60 to 150 Hz). Rather, the transition observed here appears to be via the bypass mechanism described by Ergin and White [25]. That is, the steady disturbances produced by the roughness provide an unstable basic state in which the unsteady u' disturbances rapidly grow and bring about transition. This is path D of the transition roadmap. If the measurement domain was extended, it is possible that the two lower Reynolds number cases may have generated TS waves leading to transition. The growth and breakdown of these waves would likely be affected by the steady disturbances and would therefore represent a path-B transition scenario.

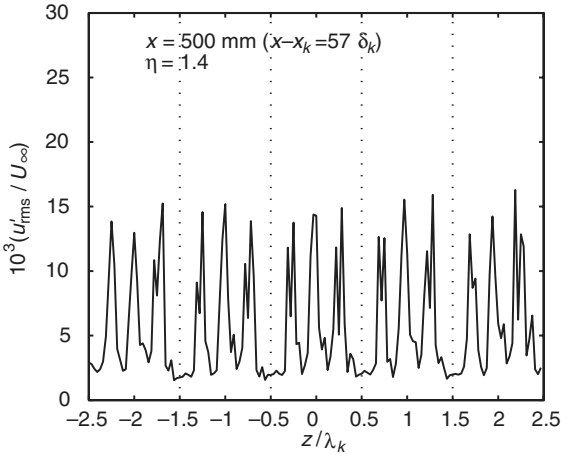

Fig. 16 Fluctuation velocity line profiles for five roughness patches for $Re_k = 301$ at $x^* = 57$ mm and $\eta = 1.4$.

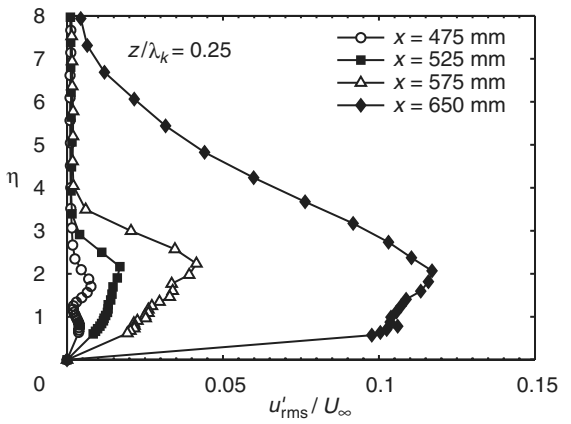

Fig. 17 Phase-lock-averaged fluctuation velocity profiles for $z/\lambda_k = 0.25$, $Re_k = 301$ at selected streamwise locations ($x^* = 29$, 86, 144, and 230).

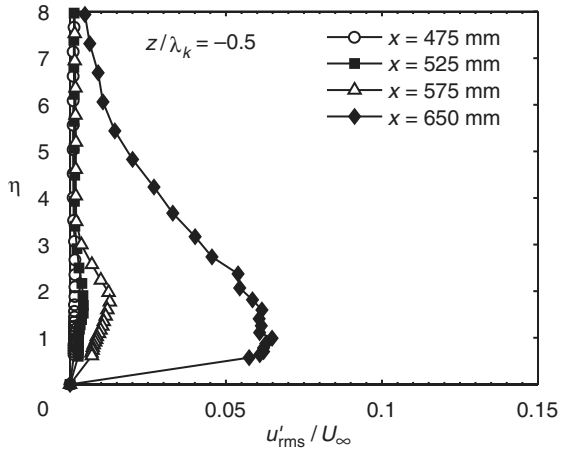

Fig. 18 Phase-lock-averaged fluctuation velocity profiles for $z/\lambda_k = \pm 0.5$, $Re_k = 301$ at selected streamwise locations ($x^* = 29$, 86, 144, and 230).

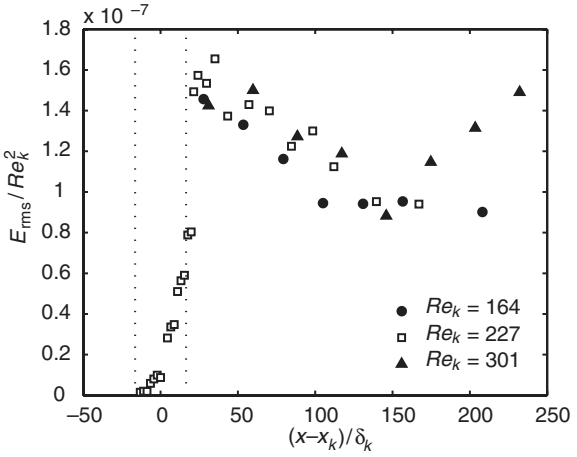

Fig. 19 Scaled disturbance-energy evolution for all three test cases. The vertical dashed lines indicate the streamwise location of the roughness.

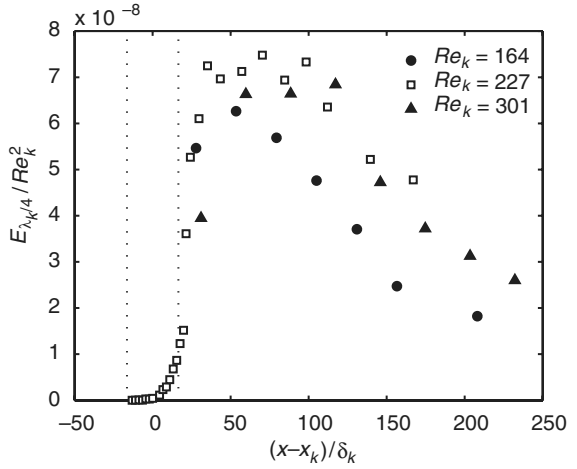

Fig. 20 Scaled $\lambda_k/4$ disturbance-energy evolution for all three test cases. The vertical dashed lines indicate the streamwise location of the roughness.

The behavior observed here is quite different than that observed by Corke et al. [31]. Corke et al. performed experiments in which distributed roughness had the effect of increasing TS-wave growth rates and accelerating the onset of transition, a path-B transition scenario. The Corke et al. experiments used two different strips of roughness and two freestream speeds, which resulted in Re_k values that ranged from 101 to 143. The u'_{rms} profiles given by Corke et al. were used as an indication of the TS nature of the eventual breakdown. It was noted that the development of an inner maximum near $\eta = 1.72$ and an outer maximum near $\eta = 5.2$ in these profiles is a strong indication of a TS mechanism. But as noted, the u'_{rms} profiles in the current experiment develop only a single maximum at approximately $\eta = 2.5$. Transition in the $Re_k = 301$ case is not via the same mechanism as the transition observed by Corke et al.

It has been observed that increasing Re_k of isolated-roughness elements results in an increased steady-disturbance magnitude [23,24,34]. The same phenomenon is observed here for distributed roughness. Scaling the disturbance energies for each test case using Re_k^2 as suggested by White et al. [24] and using the x^* normalization, the E_{rms} data collapse to a common curve, as shown in Fig. 19. It appears as if the Re_k^2 energy scaling remains appropriate for the more complicated roughness configuration considered here. A similar plot showing the normalized $E_{\lambda_k/4}$ disturbance component for the three test cases is shown in Fig. 20. The collapse of the individual mode energy is not as clean as the overall disturbance energy. This may be a consequence of the fact that $\lambda_k/4$ represents a slightly different nondimensional wavelength in each case. In the overall disturbance-energy plot (Fig. 19), this variation would not be as pronounced, because a wide range of wavelengths make up the total disturbance.

V. Conclusions

This work involves measurements of steady and unsteady boundary-layer disturbances that are generated by quasi-random distributed roughness. The intent is to extend earlier experimental work that used spanwise-periodic arrays of discrete cylindrical roughness elements to surfaces more similar to what is found in engineering practice. The use of spanwise-periodic arrays of roughness patches is an intermediate step toward performing experiments using a fully rough surface. Single-component hot-wire anemometry is employed to make boundary-layer velocity measurements above and in the wake of the distributed roughness, and the measurements are phase-lock averaged in span.

What results is a finely resolved three-dimensional grid of velocity measurements downstream of a single representative patch. The steady disturbances U' undergo transient growth for all three configurations: $U_\infty = 7.5$, 9.3, and 11.5 m/s, corresponding to $Re_k = 164$, 227, and 301, respectively. Although the total disturbance energy shows little evidence of spatial disturbance growth downstream of the roughness patches, decomposing the total disturbance energy into its spanwise components yields evidence of transient growth. In particular, the $\lambda_k/4$ and λ_k spanwise disturbance modes exhibit the transient growth phenomenon. Although the $\lambda_k/3$ mode did appear to undergo some transient growth, it is less significant than the two aforementioned modes. The $\lambda_k/2$ mode appears strictly to decay. This reinforces the finding that, in practice, disturbances are not optimal, but rather grow or decay in a manner determined by the details of that particular disturbance's receptivity process [22,24]. Finally, as in the cylindrical roughness experiments [24], it is observed that these disturbances scale with Re_k^2.

Measurements above the surface of the roughness are made in the $Re_k = 227$ configuration. The simple linear-growth, exponential-decay model for disturbance-energy evolution downstream of a cylindrical roughness element put forth in [24] is extended to the current distributed-roughness configuration. This yields a phenomenological basis for energy growth that is quadratic above the roughness and linear aft of the roughness. This argument rests on the assumption that the distributed roughness provides constant energy input per unit streamwise distance.

For the transitional configuration ($Re_k = 301$), comparison of the fluctuation velocity profiles with those of Corke et al. [31] indicates that the observed transition for this case is not due to a TS mechanism. Instead, transition is of the type observed by Ergin and White [25]. Ergin and White found that rapid transition downstream of isolated 3D elements can be characterized as a competition between unsteady-disturbance growth and stabilizing relaxation of the steady flow. This bypass mechanism is the nature of the transition that is observed in the $Re_k = 301$ configuration. Although transition is not observed for the $Re_k = 164$ and 227 cases, it is possible that the eventual transition for these cases may have been due to a TS mechanism.

Real aerodynamic surface roughness can be characterized as completely random and existing everywhere on a surface. Thus, to extend this work, the next step requires making measurements above, rather than in, the wake of a surface that is uniformly rough. To do this, it will be necessary to develop a method of separating the effects of distributed receptivity and transient growth of the resulting flow disturbances. Once this is accomplished, it may become possible to predict the transition behavior of the boundary layer, given some statistical information about the surface roughness.

Acknowledgments

This work is supported by the U.S. Air Force Office of Scientific Research under grant number FA9550-07-1-0312. R. S. Downs III acknowledges the Case School of Engineering (CSE) for its support through a CSE Graduate Fellowship. The authors wish to thank

Hillary Emer of Case Western Reserve University and Malcolm Cooke of the University of Texas, El Paso, for manufacturing the roughness sheet.

References

[1] Dryden, H. L., "Transition from Laminar to Turbulent Flow," *Turbulent Flows and Heat Transfer*, edited by C. C. Lin, Vol. 5, High Speed Aerodynamics and Jet Propulsion, Princeton Univ. Press, Princeton, NJ, 1959, pp. 3–74.

[2] von Doenhoff, A. E., and Braslow, A. L., "The Effect of Distributed Roughness on Laminar Flow," *Boundary-Layer Control*, edited by G. Lachmann, Pergamon, New York, 1961.

[3] Tani, I., "Boundary-Layer Transition," *Annual Review of Fluid Mechanics*, Vol. 1, 1969, pp. 169–196. doi:10.1146/annurev.fl.01.010169.001125

[4] Morkovin, M. V., "Panel Summary on Roughness," *Instability and Transition*, edited by M. Y. Hussaini and R. G. Voight, Vol. 1, Springer, New York, 1990, pp. 265–271.

[5] Morkovin, M. V., "On Roughness-Induced Transition: Facts, Views and Speculation," *Instability and Transition*, edited by M. Y. Hussaini and R. G. Voight, Vol. 1, Springer, New York, 1990, pp. 281–295.

[6] Schmid, P. J., and Henningson, D. S., *Stability and Transition in Shear Flows*, Springer, New York, 2001.

[7] Reshotko, E., "Transient Growth: A Factor in Bypass Transition," *Physics of Fluids*, Vol. 13, No. 5, 2001, pp. 1067–1075. doi:10.1063/1.1358308

[8] Reshotko, E., and Tumin, A., "Role of Transient Growth in Roughness-Induced Transition," *AIAA Journal*, Vol. 42, No. 4, 2004, pp. 766–770.

[9] Farrell, B. F., "Optimal Excitation of Perturbations in Viscous Shear Flow," *Physics of Fluids*, Vol. 31, Aug. 1988, p. 2093. doi:10.1063/1.866609

[10] Butler, K., and Farrell, B., "Three-Dimensional Optimal Perturbations in Viscous Shear Flow," *Physics of Fluids A*, Vol. 4, No. 8, 1992, pp. 1637–1650. doi:10.1063/1.858386

[11] Andersson, P., Berggren, M., and Henningson, D. S., "Optimal Disturbances and Bypass Transition in Boundary Layers," *Physics of Fluids*, Vol. 11, No. 1, 1999, pp. 134–150. doi:10.1063/1.869908

[12] Luchini, P., "Reynolds-Number-Independent Instability of the Boundary Layer over a Flat Surface: Optimal Perturbations," *Journal of Fluid Mechanics*, Vol. 404, 2000, pp. 289–309. doi:10.1017/S0022112099007259

[13] Tumin, A., and Reshotko, E., "Spatial Theory of Optimal Disturbances in Boundary Layers," *Physics of Fluids*, Vol. 13, No. 7, 2001, pp. 2097–2104. doi:10.1063/1.1378070

[14] Morkovin, M. V., "On the Many Faces of Transition," *Viscous Drag Reduction*, edited by C. S. Wells, Plenum, New York, 1969, pp. 1–31.

[15] Morkovin, M., Reshotko, E., and Herbert, Th., "Transition in Open Flow Systems: A Reassessment," *Bulletin of the American Physical Society*, Vol. 39, No. 9, 1994, p. 1882.

[16] Saric, W. S., Reed, H. L., and Kerschen, E. J., "Boundary-Layer Receptivity to Freestream Disturbances," *Annual Review of Fluid Mechanics*, Vol. 34, 2002, pp. 291–319. doi:10.1146/annurev.fluid.34.082701.161921

[17] Reshotko, E., and Tumin, A., "Application of Transient Growth Theory to Bypass Transition," *IUTAM Symposium on One Hundred Years of Boundary Layer Research*, edited by G. Meier and K. Sreenivasan, Springer, New York, 2006, pp. 83–93.

[18] Dryden, H. L., "Review of Published Data on the Effect of Roughness on Transition from Laminar to Turbulent Flow," *Journal of the Aeronautical Sciences*, Vol. 20, No. 7, July 1953, pp. 477–482.

[19] Klebanoff, P., Schubauer, G., and Tidstrom, K., "Measurements of the Effect of Two-Dimensional and Thee-Dimensional Roughness Elements on Boundary-Layer Transition," *Journal of the Aeronautical Sciences*, Vol. 22, 1955, pp. 803–804.

[20] Goldstein, M. E., "Scattering of Acoustic Waves into Tollmien-Schlichting Waves by Small Streamwise Variations in Surface Geometry," *Journal of Fluid Mechanics*, Vol. 154, 1985, pp. 509–529. doi:10.1017/S0022112085001641

[21] White, E. B., and Reshotko, E., "Roughness-Induced Transient Growth in a Flat-Plate Boundary Layer," AIAA Paper 2002-0138, 2002.

[22] White, E. B., "Transient Growth of Stationary Disturbances in a Flat Plate Boundary Layer," *Physics of Fluids*, Vol. 14, No. 12, 2002, pp. 4429–4439. doi:10.1063/1.1521124

[23] Fransson, J. H. M., Brandt, L., Talamelli, A., and Cossu, C., "Experimental and Theoretical Investigation of the Non-Modal Growth of Steady Streaks in a Flat Plate Boundary Layer," *Physics of Fluids*, Vol. 16, No. 10, 2004, pp. 3627–3638. doi:10.1063/1.1773493

[24] White, E. B., Rice, J. M., and Ergin, F. G., "Receptivity of Stationary Transient Disturbances to Surface Roughness," *Physics of Fluids*, Vol. 17, No. 6, 2005, p. 064109. doi:10.1063/1.1938217

[25] Ergin, F. G., and White, E. B., "Unsteady and Transitional Flows Behind Roughness Elements," *AIAA Journal*, Vol. 44, No. 11, 2006, pp. 2504–2514.

[26] Rizzetta, D. P., and Visbal, M. R., "Direct Numerical Simulations of Flow Past an Array of Distributed Roughness Elements," AIAA Paper 2006-2865, 2006.

[27] Reshotko, E., "Disturbances in a Laminar Boundary Layer Due to Distributed Surface Roughness," *Turbulence and Chaotic Phenomena in Fluids*, edited by T. Tatsumi, Elsevier, New York, 1984, pp. 39–46.

[28] von Doenhoff, A. E., and Horton, E. A., "A Low-Speed Experimental Investigation of the Effect of a Sandpaper Type of Roughness on Boundary-Layer Transition," NACA, Tech. Rep. TR 1349, 1958.

[29] Reshotko, E., and Leventhal, L., "Preliminary Experimental Study of Disturbances in a Laminar Boundary Layer Due to Distributed Roughness," AIAA Paper 81-1224, 1981.

[30] Kendall, J., "Laminar Boundary Layer Velocity Distortion by Surface Roughness: Effect upon Stability," AIAA Paper 81-0195, 1981.

[31] Corke, T. C., Bar-Sever, A., and Morkovin, M. V., "Experiments on Transition Enhancement by Distributed Roughness," *Physics of Fluids*, Vol. 29, No. 10, 1986, pp. 3199–3213. doi:10.1063/1.865838

[32] Downs, R. S., III, "Receptivity and Transient Growth of Disturbances Generated by Random Distributed Roughness," M.S. Thesis, Case Western Reserve Univ., Cleveland, OH, 2007.

[33] Saric, W. S., "Boundary-Layer Stability and Transition," *Springer Handbook of Experimental Fluid Mechanics*, edited by C. Tropea, A. L. Yarin, and J. F. Foss, Springer–Verlag, New York, 2007, pp. 886–896.

[34] White, E. B., and Ergin, F. G., "Receptivity and Transient Growth of Roughness-Induced Disturbances," AIAA Paper 2003-4243, 2003.

[35] White, E. B., and Ergin, F. G., "Using Laminar-Flow Velocity Profiles to Locate the Wall Behind Roughness Elements," *Experiments in Fluids*, Vol. 36, No. 5, 2004, pp. 805–812. doi:10.1007/s00348-003-0766-y

[36] Press, W., Teukolsky, S., Vetterling, W., and Flannery, B., *Numerical Recipes in Fortran 77*, 2nd ed., Cambridge Univ Press, New York, 2001.

A. Tumin
Associate Editor